An A-train and MERRA view of cloud, thermodynamic, and dynamic variability within the subtropical marine boundary layer

Brian H. Kahn[1], Georgios Matheou[1], Qing Yue[1], Thomas Fauchez[2], Eric J. Fetzer[1], Matthew Lebsock[1], João Martins[3], Mathias M. Schreier[1], Kentaroh Suzuki[4], and João Teixeira[1]

[1] Jet Propulsion Laboratory, California Institute of Technology, Pasadena, CA, USA
[2] NASA Goddard Space Flight Center, Greenbelt, MD, USA
[3] Instituto Português do Mar e da Atmosfera, Lisbon, Portugal
[4] Atmosphere and Ocean Research Institute, The University of Tokyo, Kashiwa, Japan

Correspondence to: Brian H. Kahn (brian.h.kahn@jpl.nasa.gov)

Abstract. The global-scale patterns and covariances of subtropical marine boundary layer (MBL) cloud fraction and spatial variability with atmospheric thermodynamic and dynamic fields remain poorly understood. We describe an approach that leverages coincident NASA A-train and the Modern Era Retrospective-Analysis for Research and Applications (MERRA) data to quantify the relationships in the subtropical MBL derived at the native pixel and grid resolution. A new method for observing four subtropical oceanic regions that capture transitions from stratocumulus to trade cumulus is demonstrated, where stratocumulus and cumulus regimes are based exclusively from infrared-based thermodynamic phase. Visible radiances are normally distributed within stratocumulus and are increasingly skewed away from the coast where trade cumulus dominates. Increases in MBL depth, wind speed and effective radius (r_e), and reductions in 700-1000 hPa moist static energy differences and 700 and 850 hPa vertical velocity, correspond with increases in visible radiance skewness. We posit that a more robust representation of the cloudy MBL is obtained using visible radiance rather than retrievals of optical thickness that are limited to a smaller subset of cumulus. The method using the combined A-train and MERRA dataset has demonstrated that an increase in r_e within shallow cumulus is strongly related to higher MBL wind speeds that further correspond to increased precipitation occurrence according to CloudSat, previously demonstrated with surface observations. Hence, the combined data sets have the potential of adding global context to process-level understanding of the MBL.

1 Introduction

Much of the uncertainty in projections of future climate is directly or indirectly related to clouds and their associated processes (IPCC AR5, 2013) including shallow marine cumuliform clouds (Bony and Dufresne, 2005). The low cloud-climate feedback is generally regarded to be positive (e.g., Clement et al., 2009). Many studies however suggest that the sign and magnitude of the feedback are cloud-type dependent (e.g., Caldwell et al. 2013; Bretherton et al., 2013; Dal Gesso et al., 2015; Stephens, 2005; Yue et al., 2017; Zelinka et al., 2012).

Using large eddy simulation (LES) experiments forced with doubled CO_2, Bretherton et al. (2013) show that the gradient of RH from the MBL to the free troposphere is a key factor that controls the shortwave cloud radiative feedback. Rieck et al.

1

(2012) used LES forced by perturbed lower tropospheric temperature profiles with fixed RH to show that an increase in surface moisture fluxes leads to a drying of the trade cumulus-topped MBL. The drying overwhelms the increased shortwave reflection from the liquid water lapse rate feedback, thus leading to reduced cloudiness and a positive shortwave cloud feedback. These mechanisms are also discussed by Nuijens and Stevens (2012) in the context of bulk theory and clearly demonstrate that free tropospheric temperature and moisture gradients act as constraints for climate change-induced surface flux changes.

While the constant RH framework is a useful concept to investigate cloud-climate feedback in simplified modeling experiments, an overall reduction of RH in the subtropical free troposphere was found in the CMIP3 (Sherwood et al., 2010; Fasullo and Trenberth, 2012) and CMIP5 (Lau and Kim, 2015) archives with a non-negligible spread in the changing magnitude and vertical structure of RH among the models. Therefore, the assumption that constant RH might hold across the diversity of subtropical cloud regimes with a changing climate is likely not valid. Medeiros and Nuijens (2016) showed that the RH gradient between the MBL and lower free troposphere is widely variable among the CMIP5 models within the trade cumulus regime. Therefore, further examination of cloud variability and the vertical structure of RH with present-day satellite and reanalysis observations is warranted.

A strong linkage between cloud amount and EIS (Wood and Bretherton, 2004), lower tropospheric stability (LTS) (Klein and Hartmann, 1993), and moist static energy differences (dMSE) between the free troposphere and surface (Kawai and Teixeira, 2010; Chung et al., 2012; Kubar et al., 2015) is well understood. Satellite observations of the MBL have revealed prodigious variations of cloud organization that span orders of magnitude over spatial and temporal scales (Cahalan et al., 1994; Wood and Hartmann, 2006; Muhlbauer et al., 2014). Even for a fixed value of cloud fraction, a large diversity of statistical variability may be observed (Kawai and Teixeira, 2012). Correlations of cloud fraction to other environmental variables are highly dependent on the time scale of comparison (e.g., Brueck et al., 2015). At present, the relationships of cloud fraction and spatial variability to larger-scale properties other than EIS/LTS remain poorly understood. Furthermore, previous work has emphasized correlations of MBL cloud properties to 500 hPa vertical velocity and RH that are averaged over monthly, seasonal, or annual time scales. Kawai and Teixeira (2010) found significant correlations for instantaneous observations of cloud inhomogeneity and the skewness of LWP to thermodynamic structure changes between 850 and 1000 hPa; the correlations are larger for LWP than with cloud fraction.

Modeling and observational studies have demonstrated that that the vertical structures of moments of conserved thermodynamic variables depend on the cloud regime (e.g., Suselj et al., 2013; Ghate et al., 2016; Zhu and Zuidema, 2009). Substantial differences exist between stratocumulus and trade cumulus in the mean, variance, skewness, and kurtosis of equivalent potential temperature θ_e, liquid water potential temperature θ_l, and vertical velocity profiles, and point to the importance of a global perspective uniquely provided by satellite and reanalysis data. The NASA A-train (Stephens et al., 2002) provides a wealth of remote sensing data about the microphysics and thermodynamics of the cloudy MBL. Reanalysis data such as the Modern Era Retrospective-Analysis for Research and Applications (MERRA; Rienecker et al., 2011) offer a

complementary set of thermodynamic and dynamic variables that help establish a larger-scale perspective for coincident remote sensing observations.

Our primary purpose is to investigate instantaneous relationships between cloud microphysical and optical properties, dynamical, and thermodynamic variables from the A-train and MERRA at the native temporal and spatial resolution of the observations. The satellite and reanalysis data each provide unique information that should ideally be combined together at the native resolution rather than relying on one instrument or reanalysis alone, or combining over time and space averages. The geophysical fields are retained at the native spatial and temporal resolution such that the instantaneous spatial "snapshots" of the cloud probability density function (pdf) are preserved and are then conditioned by available thermodynamic and dynamic variables. This approach removes the temporal variability in order to focus on the spatial variability and covariances. The statistical behavior of cloud properties, and how the thermodynamic and dynamic state variables are related to them, are thus inferred using the finest temporal and spatial resolutions available. The different instruments and reanalysis data sets are treated as "building blocks" that construct a simultaneous view of the MBL, playing on the strengths of each data set. This holistic synthesis of multivariate and multi-moment data sets may highlight aspects of MBL structure that are otherwise overlooked. The MBL structures of interest are summarized in Nuijens et al. (2009) using surface-based observations and demonstrate testable relationships between clouds, wind, humidity, and precipitation. Lastly, the approach taken herein may ultimately enhance our ability to quantify the complex time, space, and cloud regime coupling of clouds and circulation (Bony et al., 2015).

Section 2 describes the data sets used while Section 3 details the methodological approach taken in this investigation. Section 4 details the regional maps while section 5 examines the joint pdfs. We conclude in Section 6.

2 Data

The AIRS/AMSU sounding suite located onboard NASA's EOS Aqua satellite has obtained vertical profiles of temperature and water vapor at approximately 45-km horizontal resolution since September 2002 (Chahine et al., 2006). While AIRS cannot capture the sharpness of the temperature and water vapor mixing ratio gradients across the top of the MBL (Maddy and Barnet, 2008; Yue et al., 2011), the coarse-resolution vertical gradients from the surface to the lower free troposphere are obtained with high fidelity as shown in validation studies using NWP model data or radiosondes (Yue et al., 2013; Kalmus et al., 2015). The AIRS operational products also provide numerous cloud variables that include effective cloud fraction (ECF), cloud thermodynamic phase (liquid, ice, and unknown categories), and others (Kahn et al., 2014). A MBL depth estimate inferred from the height/pressure of maximum RH gradient is described and validated with radiosondes launched during the Rain in Shallow Cumulus over the Ocean (RICO) campaign in Martins et al. (2010).

The Version 5 AIRS channel 4 visible spectral radiance (0.49–0.94 μm) (Gautier et al., 2003; Aumann et al., 2006) with a nadir spatial resolution of 2.28 km is used and has units of $W/m^2/\mu m/sr$. AIRS visible band data is co-registered to the AIRS IR footprint such that 72 visible pixels are aligned within every footprint. A prototype AIRS visible cloud mask (Gautier et

al., 2003) that was developed to support earlier algorithm development efforts is also used. Although the cloud mask has not been compared directly against benchmarks such as the MODIS cloud mask, manual inspection suggests that this cloud mask tends towards clear-sky conservative and captures many shallow, broken sub-pixel cumulus clouds.

The Moderate Resolution Imaging Spectroradiometer (MODIS) instrument on EOS Aqua is capable of observing a wide variety of land, ocean, and atmospheric variables (Platnick et al., 2017) that are co-located to the AIRS FOV. We use the Collection 6 liquid phase cloud optical thickness τ and effective radius r_e retrievals from the MYD06_L2 swath product and the 1-km cloud mask from the MYD035_L2 swath product. Platnick et al. (2017) show that the r_e change between C5.1 and C6 is ±1–2μm. We have tested the differences in the pdfs between C5.1 and C6 for a subset of the data investigated and very little change in the pdfs were observed (not shown). The MODIS liquid cloud r_e is used as a proxy for precipitation and is verified with the CloudSat 2C-RAIN-PROFILE (Release 4) precipitation product (L'Ecuyer and Stephens, 2002).

The MERRA instantaneous, six-hourly, native-resolution, gridded data sets at $1/2° \times 2/3°$ (Rienecker et al., 2011) are used to assess the thermodynamic profiles derived from AIRS, assign vertical profiles of horizontal u and v wind components, and vertical profiles of pressure velocity ω in the MBL and lower free troposphere. All of the instantaneous MERRA data are spatially and temporally matched to the A-train orbit using a nearest neighbour matching approach with no time interpolation.

The matching approach uses a nearest neighbour technique weighted by the sensor spatial response function (Schreier et al., 2010). The mean, variance, and skewness of MODIS cloud properties at 1-km or 5-km resolution is retained within a larger 45-km resolution Atmospheric Infrared Sounder (AIRS)/Advanced Microwave Sounding Unit (AMSU) field of regard (FOR), while MERRA's $1/2° \times 2/3°$ resolution thermodynamic and dynamic variables are matched to the nearest AIRS/AMSU FOR.

3 Methodology

Four subtropical oceanic regions that capture transitions from stratocumulus to trade cumulus are investigated. The four regions are greatly expanded in scale from those used in Klein and Hartmann (1993) to investigate the stratocumulus-topped MBL and are listed in Table 1. While all available daytime (ascending) orbits from 1 January 2009 to 31 December 2009 were used, the remaining discussion is limited to the seasons that contain the observed peak in cloud frequency listed in Table 1 (Klein and Hartmann, 1993).

Figure 1a is an example visible image for a six-minute AIRS granule within the southeast Atlantic Ocean (SEA). The visible band captures various spatial structures of clouds. The cloud mask derived from AIRS visible bands for the same granule is shown in Fig. 1b. The cloud mask is used to narrow down the spatial sampling for the following analysis. The cloud mask likely includes instances of clear sky, but the approach only requires a coarse masking approach to filter out a majority of the clear sky pixels. We will discuss implications regarding the filtering process in Section 4.

4

Removal of pixels containing mid- and high-level clouds helps to reduce ambiguities introduced by free tropospheric clouds and also a portion of the thermodynamic and dynamic variability associated with cloudy areas of synoptic-scale waves. Figure 2 shows the AIRS infrared T_b within a clean atmospheric window at 1231 cm^{-1}, the cloud thermodynamic phase mask, three constant pressure levels of AIRS RH (700, 850, and 925 hPa), and the skewness of visible radiance for the same granule shown in Fig. 1. The cloud thermodynamic phase identifies some scattered ice in the northern portion of the granule. All pixels identified with ice are removed in the following analysis. Jin and Nasiri (2014) showed that AIRS successfully identifies the presence of ice within the AIRS FOV in excess of 90% of the time when compared to CALIPSO thermodynamic phase estimates at the pixel scale. A similar approach is taken in Nam et al. (2012) and Myers and Norris (2015) to minimize impacts from convection and synoptic-scale weather systems. Additional occurrences of $T_{b,1231} < 273$ K that potentially contain supercooled liquid phase mid-level clouds are also removed.

As the AIRS cloud phase algorithm is based on a channel selection that exploits differences in the index of refraction for liquid and ice, the cloud amount observed in the AIRS pixel is frequently small enough that the spectral signature does not trigger a positive liquid test (e.g., Jin and Nasiri, 2014). The ECF for these unknown phase cases can simultaneously be well above the sensitivity of cloud detection (validated using CALIPSO lidar, see Kahn et al., 2014). As a result, none of the phase tests are triggered even though cloud is observed within the AIRS pixel. These unknown cases line up very well with the frequency of trade cumulus in the four regions selected based on inspection of individual granule data (e.g., Figs. 1 and 2) and gridded seasonal averages (Section 4).

The AIRS liquid detections coincide with uniform stratocumulus (Fig. 1) with close to normally distributed visible radiances (lower right, Fig. 2), while unknown detections correspond well to shallow cumulus with a distinctive positively skewed visible radiance, very similar to previous results obtained using liquid water path (LWP) (Wood and Hartmann, 2006; Kawai and Teixeira, 2010). Previous investigations have used free tropospheric vertical velocity to separate cloud regime types (e.g., Bony and Dufresne, 2005; Medeiros and Stevens, 2011; Nam et al., 2012). Henceforth, the two regimes defined exclusively by *liquid* and *unknown* phase detections will be generically referred to as *stratocumulus* and *cumulus* regimes, respectively. An advantage of this instantaneous approach is that the temporal and spatial variations of cumulus and stratocumulus cloud areas are more precisely separated from each other.

For the AIRS/AMSU FORs containing MBL clouds, the coincident AIRS and MODIS geophysical fields are collocated. The AIRS ECF is averaged over the entire AIRS/AMSU FOR where clear sky is equal to a value of zero. The AIRS thermodynamic phase is averaged over cloudy AIRS FOVs only. The individual phase tests are summed and liquid is defined for values < -0.8, unknown between -0.8 to +0.8, and ice for values > +0.8. The MODIS cloud mask and τ are averaged over the entire AIRS/AMSU FOR. The MODIS r_e is averaged only over the successful retrievals that are a subset of MODIS pixels identified as containing cloud. The nearest neighbour is matched for MERRA geophysical fields at a similarly sized spatial resolution. The mean, standard deviation, and skewness of MODIS and AIRS FOV properties are then calculated for each AIRS/AMSU FOR separately. Therefore, multiple satellite instrument and reanalysis observations at

multiple spatial scales can be linked together through joint pdfs for a large combination of statistical moments. These data serve as the basis of the following investigation.

4 Regional spatial averages

Regional-scale, seasonal averages are calculated from the pixel-scale data described in Section 3 for 90 daytime (130 pm equatorial crossing time) snapshots and are then re-gridded to 1°×1° spatial resolution and help facilitate comparisons to previous studies. Figure 3 shows the visible radiance skewness for JJA in the NEP and NEA regions, and SON in the SEP and SEA regions, with an overlay of AIRS total ECF. The coastal stratocumulus radiances are distributed approximately normally while the radiances are positively skewed away from the coast where disorganized cumulus dominates (e.g., Wood and Hartmann, 2006). Contours of the magnitude of radiance skewness closely align to the magnitude of ECF in cumulus while much less so in proximity to the coast within stratocumulus. Very poor spatial correspondence between radiance skewness and the mean value of MODIS cloud fraction was found (not shown) and is consistent with low correlations between GOES derived cloud fraction and LWP noted by Kawai and Teixeira (2010) in the SEP region. Interestingly, the average radiance skewness is larger and ECF is smaller in the NEA than the other three regions and is consistent with other satellite observations (Klein and Hartmann, 1993; Rossow and Schiffer, 1999) and ship-based observations (Wood, 2012). The patterns of radiance skewness shown in Fig. 3 also resemble typical climatological patterns of cloud sizes reported in Wood and Field (2011) and cloud texture as viewed from the Multi-angle Imaging SpectroRadiometer (MISR) (Zhao et al., 2016).

Values of MODIS total water path (TWP) skewness do not show a clear transition from normally distributed to positively skewed values in Weber et al. (2011). This further motivates the removal of mid- and high-level cloud occurrences using the AIRS phase mask that comprise anywhere from 4 to 18% of the total number of FOVs depending on the region of study (Table 1). The total number of collocated data points within each region is roughly ~180,000. However, the AIRS and MODIS cloud fields have smaller spatial resolutions that are aggregated to the AIRS/AMSU field of regard, and the raw counts for these fields number in the millions. Oreopoulos and Cahalan (2005) show that the inhomogeneity parameter calculated from MODIS LWP, rather than TWP, is most homogeneous near the coast and indicates increasing heterogeneity that extends into the cumulus regimes. We argue that the results of Oreopoulos and Cahalan (2005) are more definitive than those shown in Weber et al. (2011) and more closely resemble the gradients and magnitudes contained within Fig. 3.

There are several factors that contribute to relationships between ECF and the various moments of radiance. A reduced ECF and increased radiance skewness (Fig. 3) may indicate smaller cloud sizes but is probably not universally true. If the cloud optical thickness is decreased, the ECF is also decreased from reductions in cloud emissivity even though cloud coverage itself may remain constant. (Recall that the ECF is a convolution of emissivity and cloud fraction.) If the cloud optical thickness is fixed, the cloud emissivity remains fixed even though the cloud coverage itself and ECF could be decreased. The ECF could also be decreased (increased) if small cloud elements become more widely spaced (packed together)

assuming the cloud sizes of the individual cumulus elements remain the same. With respect to the visible radiances, the radiance is decreased if cloud elements become smaller than the nominal 2.2 km pixel size assuming the optical thickness of the cloud elements does not change. Therefore, if an increased proportion of a cloud population with normally distributed radiances becomes subpixel in size, one would expect a shift towards positive skewness. If cloud distributions are spatially resolved, an increased skewness radiance is still entirely possible if the optical thickness of cloud distributions is skewed itself. However, in this investigation, the skewness of the MODIS optical thickness is less skewed at low ECF than visible radiance (not shown). This suggests that the skewness in the visible radiance at low ECF at least partially arises from smaller cloud sizes.

The mean MBL depth (Fig. 4) reaffirms a characteristic transition from shallow MBLs (920–970 hPa) near the coast to deeper MBLs (830–880 hPa) to the west and is a well-observed feature of the stratocumulus to cumulus transition previously observed by Karlsson et al. (2010), Teixeira et al. (2011), and others. Closest to the coast, the MBL is shallowest in the NEA and slightly deeper in the NEP. The SEA and SEP are deeper than their NH counterparts with SEP the deepest. The SEP MBL depths agree with VOCALS-REx in situ radiosonde-derived temperature inversion base heights described by Bretherton et al. (2010). Furthermore, the inter-regional differences in MBL depth show consistency with global positioning system-radio occultation (GPS-RO) data described by Chan and Wood (2013).

Differences in the moist static energy (dMSE) between 700 and 1000 hPa are calculated following the approach outlined by Kubar et al. (2012) and are also shown in Fig. 4. The dMSE is calculated from quality-controlled AIRS soundings (PGood ≥ 1000 hPa) and is nearly identical to estimates from ERA-Interim shown by Kubar et al. (2012). The magnitude of dMSE is larger and positive near the coast in the SH compared to the NH and is somewhat reduced in the NEA region. Yue et al. (2011) showed that values of EIS and LTS obtained from AIRS soundings are lower in the NEA compared to the other three regions and are also consistent with Fig. 4.

Seasonal averages of AIRS RH_{700} with an overlay of the corresponding MERRA-AIRS RH_{700} differences are shown in Fig. 5. Wind vectors depict the mean horizontal flow. Overall, RH_{700} in the SH is lower than the NH while the NEA is the moistest of the four regions and SEP the driest. MERRA is on average moister than AIRS by ~5% in the NH, nearly identical to AIRS in the SEA, and a much more spatially heterogeneous difference is observed in the SEP from the coastal proximity westward between 8–12°S.

Bretherton et al. (2010) demonstrate that the free troposphere in the SEP westward of 75°W is characteristically very dry (0.1 g kg^{-1}) with sporadic filaments of moist air (as high as 3-6 g kg^{-1}) up to an altitude of 2.5 km. In addition, these moist filaments have been observed with GPS-RO refractivity profiles by von Engeln et al. (2007). The vertical structure of RH obtained from VOCALS-REx radiosondes implies a well-mixed MBL near the coast with MBL decoupling west of 80°W. Myers and Norris (2015) showed that 700 hPa is drier in the SH subtropics compared to the NH using ERA-Interim data. When GCMs are sampled for RICO-like conditions using representative mid-tropospheric large-scale vertical velocities as in Medeiros and Stevens (2011), a dry bias is obtained above the MBL in comparison to a composite of RICO radiosondes.

The seasonal averages of AIRS RH_{850}, and the corresponding MERRA-AIRS RH_{850} differences, are larger than that found for RH_{700} (Fig. 6) and are due to temperature and water vapor weighting function widths on the order of 2–3 km (Maddy and Barnet, 2008).

In summary, the seasonal averages exhibit realistic three-dimensional spatial morphologies and gradients and show consistency with MERRA RH in the subtropical MBL. The MBL depth and seasonal variations (not shown) agree with GPS-RO (Chan and Wood, 2013). The AIRS-derived dMSE between 700 and 1000 hPa agrees with ERA-Interim (Kubar et al., 2012). The radiance skewness is strongly related to dMSE (Kawai and Teixeira, 2012). The AIRS ECF distributions closely correspond to well-established climatologies of cloud amount (e.g., Klein and Hartmann, 1993; Rossow and Schiffer, 1999; Wood, 2012). The vertical structure of the horizontal wind flow well represents known climatological patterns in the MBL and lower free troposphere. While the variability within each region and between the four regions is consistent with previous studies, the physical reasons for these differences are beyond the scope of the current investigation.

5 Multivariate and multi-moment pdfs

5.1 Dimensionality of pdfs

Choosing an ideal subset of variables and statistical moments to form the basis of joint histograms is a challenge. Motivated in large part to link cloud and thermodynamic properties derived from infrared and visible bands, we describe six variable combinations. The natural log frequency of occurrence is shown in gray scale from black to white and MBL depth is superimposed as contours (Fig. 7).

The MBL depth exhibits clearer patterns in the ECF dimension (Fig. 7a,c) rather than the cloud fraction dimension (Fig. 7b,d). The latter is more compressed and the gradients are weaker in both dimensions. The MBL depth is deepest for lower values of ECF, τ, and visible radiance. In addition, the MBL depth also decreases for the most reflective clouds at a given value of ECF while this behaviour is not observed for τ. An additional population of sub-pixel cumulus clouds is captured within the radiance data that is not captured in τ data. The two other panels (Fig. 7e,f) highlight the challenges with the choice of dimensionality. In the case of radiance versus τ, while there is a strong correlation in the occurrence frequency within the more reflective clouds, the structure in the MBL depth is much less clear. In the case of cloud fraction versus ECF, the occurrence frequency is much more poorly correlated and scattered, while the MBL depth shows less structure in either dimension.

We will use radiance versus ECF (Fig. 7a) in the remainder of this work. We are not advocating that the dimensional choices made are optimal. Instead, the results motivate the use of satellite and reanalysis data building from native resolution, pixel-scale, temporally instantaneous coincidences.

5.2 Regional similarity in MBL depth

The frequencies of AMSU FORs that contain stratocumulus and cumulus are listed in Table 1. The largest differences in the gradients between stratocumulus and cumulus are found in the NEP (Fig. 8a,e), while the smallest differences are found in the NEA (Fig. 8c,g). The MBL depth is several 10s of hPa shallower in stratocumulus (Fig. 8a-d) compared to cumulus (Fig.
5 8e-h) in all four regions for almost every possible combination of radiance and ECF. We can conclude that the cloud amount and shortwave reflected radiation act independently of MBL depth. A small population of shallow MBL depths for ECF > 0.9 is found in cumulus (Fig. 8e-h) and is a consequence of a few stratocumulus clouds that fail to exhibit a large enough T_b signature to trigger liquid phase tests (e.g., Kahn et al., 2011; 2014). The two cloud regimes therefore should not be considered mutually exclusive of each other.

10 A significant increase in MBL depth with increasing radiance is found in cumulus with a stronger relationship in the NH compared to the SH (Fig. 8e-h) at a fixed value of ECF. This is partly a result of a deeper MBL in the SEP and SEA near the coastline (Fig. 4). The exception is that the NEP, SEP, and SEA show a decrease for the most reflective clouds except for the NEA. Generally speaking the NEA is the largest outlier of the four regions for all radiance moments shown for MBL depth in Fig. 8 and is affected more by the midlatitudes than other regions. The MBL depth gradients have an approximately linear
15 relationship with the standard deviation of radiance (Fig. 8i-l) unlike the average radiance (Fig. 8e-h). The MBL is deepest for the largest values of the standard deviation at almost all values of ECF in all four regions. This suggests that the largest values of average radiance in Fig. 8e-h are uniform in spatial structure and have some of the lowest standard deviations (Fig. 8e-h).

The radiance skewness is shown in Fig. 8m-p. There are several important features to describe. First, the MBL depth is
20 shallower for normally distributed radiance and a sharp increase in MBL depth with increasing positive skewness is consistent with Figs. 3 and 4. Second, the change in MBL depth is somewhat greater for an identical increase in radiance skewness when compared to τ skewness (not shown). Third, the cumulus occurrences at low ECF for positive skewness > 1 are mostly absent in the τ data (not shown) but are very common in radiance data. We argue that this discrepancy has an important impact on the interpretation of the trade cumulus climatology. The gradient of MBL depth in the dimension of
25 increasing positive skewness at low values of ECF is much greater in the radiance data where the highest data counts are found. We posit that the radiance data contain more subpixel cumulus missing in the τ data. Fourth (not shown), the AIRS cloud mask filter (Fig. 1b) is removed in order to retain all values of radiance (clear and cloudy) in the joint pdf. While the patterns of radiance skewness and MBL depth are not significantly altered when applying the cloud mask filter, many more counts with normally distributed radiances appear that indicates some leakage of weak clear-sky surface reflection. We
30 conclude that there is a much bigger difference between the cloud mask-filtered radiance and τ, rather than between the filtered and non-filtered variants of radiance, implying a robust interpretation. Fifth, the MBL depth contours change more rapidly with skewness of τ or radiance rather than with the mean value of τ or radiance, consistent with the findings of Kawai and Teixeira (2010) where a tighter correlation with LWP skewness compared to average LWP was found.

9

Figure 9 shows that the dMSE in the SEP is positive in sign and largest in magnitude for larger values of ECF and normally distributed radiance (other regimes are similar and are not shown). In the case of radiance skewness, contours of constant dMSE track closely to the occurrence frequency through much of the joint pdfs, with a reduction of dMSE to values less than zero at a fixed value of ECF as positively skewed radiances increases. This behavior is similar to MBL depth (Fig. 8f) and

5   suggests that instantaneous values of dMSE correlate well with small-scale cloud variability. This is not inconsistent with LTS and dMSE correlating well with larger-scale atmospheric thermodynamic structure on much longer time scales. Kawai and Teixeira (2012) showed that the skewness of LWP varies from +1 to +2 for cloud amounts of 90–100%, and up to +1.5 to +3.5 for cloud amounts < 30%. Furthermore, Kawai and Teixeira (2010) found that the highest correlations occur between LWP homogeneity, skewness and kurtosis to different measures of temperature and moisture differences from the surface to

10   850 hPa, rather than to values of EIS and LTS.

5.3 Relating meteorology and microphysical processes

Nuijens et al. (2009) describe Rain in Cumulus over the Ocean (RICO) field campaign observations that illustrate fundamental physical relationships between cloud cover, wind speed and direction, the vertical structure of RH, and precipitation frequency and intensity within precipitating shallow trade cumulus. The observations can be grouped into three

15   fairly distinct cumulus regimes: (i) low cloud fraction with little to no precipitation characterized by low values of u and a drier MBL; (ii) an increase in cloud fraction with some light precipitation characterized by low values of u and elevated RH between 800-1000 hPa; (iii) a further increase in cloud fraction with light precipitation and some isolated heavier events characterized by higher values of u and a large increase in RH between 650-900 hPa. A key observational difference among the three regimes is the variation of RH within the MBL (800-1000 hPa), and near the top of the MBL extending into the

20   lower free troposphere (650-900 hPa). The width of these layers is similar to the AIRS 700 and 925 hPa temperature and specific humidity weighting functions. Even though the RICO observations do not fall within any of the four regions listed in Table 1, Medeiros and Nuijens (2016) show that the observational site is applicable to the trade regime as a whole across the globe. Thus our approach for the remainder of the investigation is to determine if similar relationships shown in Nuijens et al. (2009) exist in cumulus for the regions listed in Table 1.

25   Figure 10 shows the MODIS derived r_e for stratocumulus (Fig. 10a-d) and cumulus (Fig. 10e-p) that are limited to successful retrievals (no PCL pixels are included). There are several prominent features in the histograms. First, the stratocumulus r_e is about 11 to 12 μm throughout most of the pdf in all four regions. An exception is the increase of r_e by several μm when average radiance and ECF are reduced (Fig. 10a-d). While these particular MODIS pixels were successful, cloud horizontal inhomogeneity causes larger r_e within this population of clouds because of the plane parallel homogeneous bias (Cho et al.,

30   2015; Zhang et al., 2016). Cloud inhomogeneity may also lead to significant 3-D radiative transfer effects but these tend to cause both larger and smaller r_e in similar proportions (Zhang et al., 2012). Second, the NEA region (Fig. 10g) is most dissimilar to the other three regions for average (Figs. 10e-h), standard deviation (Fig. 10i-l) and skewness (Fig. 10m-p). Third, r_e is largest along the axis of maximum counts with values upwards of 16 to 20 μm in the SEP, 15-18 μm in the SEA,

10

and 14–17 μm in the NEP. The largest values in the NEA are confined to the most skewed radiances unlike the other three regions. Fourth, in the cleaner SH, the values of r_e appear to be more tightly coupled to cloud microphysical processes that respond to changing wind speed and a deepening MBL. Fifth, the variations of r_e with the standard deviation of radiance (Fig. 10i-l) are more nonlinear than in the case of MBL depth (Fig. 8i-l). This shows that the relationship between radiance

5   moments and different physical quantities is not the same.

One general interpretation of the larger r_e in cumulus (Fig. 10e-h) when contrasted to stratocumulus (Fig. 10a-d) is that it is caused by increased inhomogeneity of cumulus (Zhang et al., 2012), retrieval failures and partly cloudy pixels (Cho et al., 2015), and view angle biases (e.g., Liang et al., 2015) that are further coupled together with other factors at play (Zhang et al., 2016). The aforementioned issues may still impact a successful r_e retrieval. However, we offer evidence that the increase

10   in r_e is also consistent with environmental variability that in turn is consistent with droplet growth and precipitation. The contours of r_e correspond very closely to the magnitude of the u-component of wind speed at 925 hPa (u_{925}) (see Fig. 12) and other levels in the MBL (not shown), suggesting a link between cloud droplet growth, light rain, and dynamical variability. The somewhat larger r_e in the SH is consistent with droplet growth in a cleaner environment (Suzuki et al., 2010a,b). Successful retrievals may be more frequently precipitating, either because of larger r_e in the cloud, or because the plane

15   parallel homogeneous bias is larger in precipitating clouds.

To determine if the elevated r_e along the axis of maximum counts is associated with increased precipitation frequency, collocated matchups of the CloudSat precipitation rate are used to determine which AMSU FOVs contain occurrences of precipitation. Figure 11 shows results for the SEP region. The radiance skewness for the full AIRS/AMSU/MODIS swath in Fig. 10n is restricted to the CloudSat ground track in Fig. 11a. The counts are reduced by a factor of ~30 as expected. There

20   are some subtle changes in the r_e distribution showing an increase of 2-3 μm with increasing skewness at a fixed value of ECF. Figure 11b shows the proportion of the pdf that contains at a minimum the natural log(2) counts of precipitation occurrence within each bin. About 20-50% of the AMSU FOVs are precipitating according to CloudSat within the pdf of Fig. 11a. The precipitation frequency is consistent with Rapp et al. (2013) where up to 40% of clouds precipitate in the cumulus regime. Little to no precipitation occurs outside of the central portion of the pdf in Fig. 11a. The highly skewed

25   cumulus with ECF<0.2 appear to be exhibiting large r_e biases due to visible radiance inhomogeneity (Cho et al., 2015; Zhang et al., 2016). We also point out that the population of clouds detected by CloudSat that have ECF>0.95 (Fig. 11b) are associated with very little precipitation and is consistent with the spatial distributions described by Rapp et al. (2013).

Figure 12 shows $\theta_{e,700}$, u_{925}, ω_{700}, and ω_{925}. The θ_{700} (not shown) is nearly identical among all regions with θ_{700}=314 K ± 1 K. Thus, the structure in $\theta_{e,700}$ (Fig. 12a-d) is driven by variations in specific humidity. For a fixed value of ECF, the clouds

30   with the lowest and highest values of radiance are associated with moistening of the lower free troposphere. Using climatological averages, Myers and Norris (2015) show that shortwave observations from CERES, cloud fraction estimates from ISCCP and CALIPSO, and RH_{700} and ω_{700} from ERA-Interim reflect aspects of Fig. 12 and, namely, that more reflected shortwave is associated with increased cloud fraction and decreased ω_{700}.

The highest values of $\theta_{e,925}$ (not shown) occur along the axis of highest counts while reductions in $\theta_{e,925}$ occur for the least and most reflective clouds at a fixed value of ECF. This is the case for the NEP, SEP, and SEA, but the NEA is an outlier and shows a constant increase as seen with RH and MBL depth. Unlike 700 hPa, θ_{925} is more variable (not shown) between the four regions but is generally 2 K or less.

5 The u_{925} is largest (Fig. 12e-h) when the pdf has the largest counts and very closely resembles r_e in Fig. 10e-h. The subtle differences in the contours in Fig. 10e-h and Fig. 12e-h align very well, suggesting a tight correlation between the two parameters. The magnitude of u_{925} is larger than u_{700} (not shown) consistent with RICO (Nuijens and Stevens, 2009). The ω_{700} fields (Fig. 12i-l) exhibit minimal correspondence with average radiance and ECF in the NH regimes with a weak correspondence in the average radiance in the SH regions. The ω_{925} fields (Fig. 12m-p) show larger gradients in all four

10 regions. The ω_{925} decreases with increasing radiance in all regions similar to that shown in Myers and Norris (2015), with a slightly noisier pattern in ω_{925} observed in the NH regimes. The decrease of ω_{925} with increasing radiance is consistent with a deeper MBL (Fig. 8e-h) and larger τ. Where u_{925} (Fig. 12e-h) increases, ω_{925} (Fig. 12m-p) decreases and RH_{925} increases (not shown). The largest values of r_e (Fig. 10e-h) also correspond to the above tendencies, consistent with the concept of more frequent precipitating clouds within a windier and deeper MBL (Nuijens and Stevens, 2012).

15 The joint pdfs imply simultaneous increases in $\theta_{e,700}$, $\theta_{e,925}$ (and by extension RH_{700} and RH_{925}), u_{925}, and ECF in three of the four regions investigated (NEP, SEP, and SEA) with a particularly strong relationship between u_{925} and r_e. The NEA is somewhat of an outlier although this is based on one seasons' worth of data during 2009. There is much variability across the trade cumulus regime as it should~~is~~ not be treated as a single homogeneous entity.

6 Summary and Conclusions

20 The global-scale relationships and coupling of cloud fraction and spatial variability to thermodynamic and dynamic properties of the atmosphere remain poorly understood (Bony et al., 2015). The NASA A-train (Stephens et al., 2002) provides a wealth of remote sensing data about the microphysics and thermodynamics of the cloudy MBL. The Modern Era Retrospective-Analysis for Research and Applications (MERRA; Rienecker et al., 2011) offers a complementary set of thermodynamic and dynamic variables that helps establish context for coincident remote sensing observations. The synergy

25 between satellite and reanalysis data at the native spatial and temporal resolutions available has not been fully exploited to date. We describe a new approach that leverages coincident reanalysis and remote sensing data at the native resolution of the observations. The spatial variability of clouds, and the relationship to thermodynamic and dynamic state variables, is thus inferred using the finest temporal and spatial resolutions available.

Four subtropical oceanic regions that capture transitions from stratocumulus to trade cumulus are investigated. We define

30 two regimes based exclusively on *liquid* and *unknown* cloud thermodynamic phase detections with the AIRS instrument, and generically refer to them as *stratocumulus* and *cumulus* regimes, respectively. The mean, standard deviation, and skewness

of MODIS and AIRS FOV cloud properties and visible radiances are calculated for each AIRS and MERRA temperature and humidity observation.

As with previous findings, coastal stratocumulus radiances are approximately normally distributed while the radiances are positively skewed away from the coast where disorganized cumulus dominates. The radiance skewness closely aligns to the magnitude of AIRS effective cloud fraction (ECF) in cumulus with less correspondence in stratocumulus. Strong (poor) spatial correspondence between radiance skewness and AIRS ECF (MODIS cloud fraction) was found suggesting infrared-based ECF is a potentially valuable and unappreciated diagnostic for MBL cloud characterization. The mean MBL depth derived from AIRS (Martins et al., 2010) shows a characteristic transition from shallow MBLs (920–970 hPa) near the coast to deeper MBLs (830–880 hPa) away from the coast and is a well-observed feature of the stratocumulus to cumulus transition (e.g., Teixeira et al., 2011). The AIRS-derived moist static energy differences (dMSE) between 700 and 1000 hPa agree very well with ERA-Interim (Kubar et al., 2012). We find that the radiance skewness is strongly related to the magnitude of dMSE as previously found by Kawai and Teixeira (2012). The MBL depth is shallower for stratocumulus than cumulus for almost all values of visible radiance and ECF.

The change in MBL depth is somewhat greater for an identical increase in radiance skewness when compared to τ skewness. The population of cumulus occurrences at low ECF for positive skewness > 1 are mostly absent in the τ data but are very common in radiance data. This highlights the importance of understanding the sampling from derived Level 2 products compared to Level 1 radiances that may capture a fuller range of the geophysical state in different cloud regimes.

The r_e in stratocumulus is about 11 to 12 μm for most values of radiance and ECF in all four regions of study. For cumulus, r_e ranges anywhere from 12 to 20 μm, with larger r_e for increasing positive skewness especially when ECF is small. The values of r_e appear to be tightly coupled to cloud microphysical processes that respond to changing MBL wind speed and a deepening MBL. We argue that for these successful MODIS retrievals, the increase in r_e is consistent with increased droplet growth and hence precipitation occurrence. This may be caused by larger r_e in the cloud itself or that precipitating clouds are associated with an increased subpixel inhomogeneity that leads to the plane parallel homogeneous bias; this topic warrants further investigation. In the SEP region, the elevated values of r_e that correspond with the increased u_{925} are more frequently precipitating according to CloudSat.

The Rain in Cumulus over the Ocean (RICO) observations provide an important multi-parameter testing benchmark (Nuijens et al., 2009). These results are generalized into three types of shallow precipitating cumulus regimes observed during RICO. The joint pdfs imply simultaneous increases in $\theta_{e,700}$, $\theta_{e,925}$, u_{925}, and ECF in three of the four regions investigated (NEP, SEP, and SEA) with a strong correspondence between u_{925} and r_e. The NEA less clearly follows these behaviors and is an outlier, although this is based on one seasons' worth of data during 2009.

Future work will expand to other cloud regimes, additional data sets, and multiple years of data. A similar approach with numerical model output should also be attempted using temporal snapshots of similar geophysical fields. We expect that this

13

approach will be especially useful for linking cloud microphysics together with the thermodynamic and dynamic state of the atmosphere at the process scale.

Acknowledgments

References

Aumann, H. H., Broberg, S., Elliott, D., Gaiser, S., and Gregorich, D.: Three years of Atmospheric Infrared Sounder radiometric calibration validation using sea surface temperatures, J. Geophys. Res., 111, D16S90, doi:10.1029/2005JD006822, 2006.

Bony, S. and Dufresne, J. L.: Marine boundary layer clouds at the heart of tropical cloud feedback uncertainties in climate models, Geophys. Res. Lett., 32, L20806, doi:10.1029/2005GL023851, 2005.

Bony, S., Stevens, B., Frierson, D. M. W., and Coauthors: Clouds, circulation and climate sensitivity, Nat. Geosci., 8, 261–268, doi:10.1038/ngeo2398, 2015.

Bretherton, C. S., Wood, R., George, R. C., Leon, D., Allen, G., and Zheng, X.: Southeast Pacific stratocumulus clouds, precipitation and boundary layer structure sampled along 20°S during VOCALS-REx, Atmos. Chem. Phys., 10, 10639–10654, 2010.

Bretherton, C. S., Blossey, P. N., and Jones, C. R.: Mechanisms of marine low cloud sensitivity to idealized climate perturbations: A single-LES exploration extending the CGILS cases, J. Adv. Model. Earth Sys., 5, 316–337, doi:10.1002/jame.20019, 2013.

Brueck, M., Nuijens, L., and Stevens, B.: On the seasonal and synoptic time-scale variability of the North Atlantic trade wind region and its low-level clouds, J. Atmos. Sci., 72, 1428–1446, 2015.

Cahalan, R. F., Ridgway, W., Wiscombe, W. J., and Bell, T. L.: The albedo of fractal stratocumulus clouds, Mon. Wea. Rev., 51, 2434–2455, 1994.

5   Caldwell, P. M., Zhang, Y., and Klein, S. A.: CMIP3 subtropical stratocumulus cloud feedback interpreted through a mixed-layer model, J. Climate, 26, 1607–1625, 2013.

Chahine, M. T., Pagano, T. S., Aumann, H. H., and Coauthors: The Atmospheric Infrared Sounder (AIRS): Improving weather forecasting and providing new insights into climate, B. Am. Meteor. Soc., 87, 911–926, doi:10.1175/BAMS-87-7-911, 2006.

10   Chan, K. M., and Wood, R.: The seasonal cycle of planetary boundary layer depth determined using COSMIC radio occultation data, J. Geophys. Res. Atmos., 118, 12,422–12,434, doi:10.1002/2013JD020147, 2013.

Cho, H.-M., et al.: Frequency and causes of failed MODIS cloud property retrievals for liquid phase clouds over global oceans, J. Geophys. Res. Atmos., 120, 4132–4154, 2015, doi:10.1002/ 2015JD023161.

Chung, D., Matheou, G., and Teixeira, J.: Steady-state large-eddy simulations to study the stratocumulus to shallow cumulus

15   cloud transition, J. Atmos. Sci., 69, 3264–3276, doi:10.1175/JAS-D-11-0256.1, 2012.

Clement, A. C., Burgman, R., and Norris, J. R.: Observational and model evidence for positive low-level cloud feedback, Science, 325, 460–464, doi:10.1126/science.1171255, 2009.

Dal Gesso, S., Siebesma, A. P., and de Roode, S. R.: Evaluation of low-cloud climate feedback through single-column model equilibrium states, Q. J. Royal Met. Soc., 141, 819–832, doi:10.1002/qj.2398, 2015.

20   Fasullo, J. T., and Trenberth, K. E.: A less cloudy future: The role of subtropical subsidence in climate sensitivity, Science, 338, 792–795, doi:10.1126/science.1227465, 2012.

Fetzer, E. J., Lambrigtsen, B. H., Eldering, A., Aumann, H. H., and Chahine, M. T.: Biases in total precipitable water vapor climatologies from Atmospheric Infrared Sounder and Advanced Microwave Scanning Radiometer, J. Geophys. Res., 111, D09S16, doi:10.1029/2005JD006598, 2006.

25   Gautier, C., Shiren, Y., and Hofstadter, M. D.: AIRS/Vis Near IR instrument, IEEE Trans. Geosci. Remote Sens., 41, 330–342, 2003.

Ghate, V. P., Miller, M. A., and Zhu, P.: Differences between nonprecipitating tropical and trade wind marine shallow cumuli, Mon. Wea. Rev., 144, 681–701, 2016.

IPCC: Climate Change 2013: The Physical Science Basis. Contribution of Working Group I to the Fifth Assessment Report

30   of the Intergovernmental Panel on Climate Change, edited by T. F. Stocker, et al., 1535 pp., Cambridge Univ. Press, Cambridge, U. K., and New York, doi:10.1017/CBO9781107415324, 2013.

Jin, H., and Nasiri, S. L.: Evaluation of AIRS cloud-thermodynamic-phase determination with CALIPSO, J. Appl. Meteor. Climatol., 53, 1012–1027, 2014.

Kahn, B. H.,. Nasiri, S. L, Schreier, M. M., and Baum, B. A.: Impacts of subpixel cloud heterogeneity on infrared thermodynamic phase assessment, J. Geophys. Res., 116, D20201, doi:10.1029/2011JD015774, 2011.

Kahn, B. H., Irion, F. W., Dang, V. T., and Coauthors: The Atmospheric Infrared Sounder Version 6 cloud products, Atmos. Chem. Phys., 14, 399–426, 2014.

5   Kalmus, P., Wong, S., and Teixeira, J.: The Pacific subtropical cloud transition: A MAGIC assessment of AIRS and ECMWF thermodynamic structure, IEEE Geosci. Remote Sens. Lett., 12, 1586–1590, doi:10.1109/LGRS.2015.2413771, 2015.

Karlsson, J., Svensson, G., Cardoso, S., Teixeira, J., and Paradise, S.: Subtropical cloud-regime transitions: boundary layer depth and cloud-top height evolution in models and observations, J. Appl. Meteor. Climatol., 49, 1845–1858, 2010.

10 Kawai, H., and Teixeira, J.: Probability density functions of liquid water path and cloud amount of marine boundary layer clouds: Geographical and seasonal variations and controlling meteorological factors, J. Climate, 23, 2079–2092, 2010.

Kawai, H., and Teixeira, J.: Probability density functions of liquid water path and total water content of marine boundary layer clouds: Implications for cloud parameterization, J. Climate, 25, 2162–2177, 2012.

Klein, S. A., and Hartmann, D. L.: The seasonal cycle of low stratiform clouds, J. Climate, 6, 1587–1606, 1993.

15 Kubar, T. L., Waliser, D. E., Li, J.-L., and Jiang, X.: On the annual cycle, variability, and correlations of oceanic low-topped clouds with large-scale circulation using Aqua MODIS and ERA-Interim, J. Climate, 25, 6152–6174, 2012.

Kubar, T. L., Stephens, G. L., Lebsock, M., Larson, V. E., and Bogenschutz, P. A.: Regional assessments of low clouds against large-scale stability in CAM5 and CAM-CLUBB using MODIS and ERA-Interim reanalysis data, J. Climate, 28, 1685–1706, 2015.

20 L'Ecuyer, T. S., and Stephens, G. L.: An estimation-based precipitation retrieval algorithm for attenuating radars. *J. Appl. Meteor.*, **41**, 272–285, 2002, doi:10.1175/1520-0450(2002)041<0272:AEBPRA>2.0.CO;2.

Lau, K. M., and Kim, K.-M.: Robust Hadley circulation changes and increasing global dryness due to CO_2 warming from CMIP5 model projections, Proc. Natl. Acad. Sci., 112, 3630–3635, 2015.

Liang, L., Di Girolamo, L., and Sun, W: Bias in MODIS cloud drop effective radius for oceanic water clouds as deduced
25 from optical thickness variability across scattering angles, J. Geophys. Res. Atmos., 120, 7661–7681, 2015, doi:10.1002/2015JD023256.

Maddy, E. S., and Barnet, C. D.: Vertical resolution estimates in Version 5 of AIRS operational retrievals, IEEE Trans. Geosci. Remote Sens., 46, 2375–2384, 2008.

Martins, J. P. A., Teixeira, J., Soares, P. M. M., Miranda, P. M. A., Kahn, B. H., Dang, V. T., Irion, F. W., Fetzer, E. J., and
30 Fishbein, E.: Infrared sounding of the trade-wind boundary layer: AIRS and the RICO experiment, Geophys. Res. Lett., 37, L24806, doi:10.1029/2010GL045902, 2010.

Medeiros, B. P., and Stevens, B.: Revealing differences in GCM representations of low clouds, Clim. Dyn., 36, 385–399, 2011.

Medeiros, B. P., and Nuijens, L.: Clouds at Barbados are representative of clouds across the trade wind regions in observations and climate models, Proc. Natl. Acad. Sci., 113(22):E3062-70, 2016, doi: 10.1073/pnas.1521494113.

Muhlbauer, A., McCoy, I. L., and Wood, R.: Climatology of stratocumulus cloud morphologies: microphysical properties and radiative effects, Atmos. Chem. Phys., 14, 6695–6716, 2014.

5   Myers, T. A., and Norris, J. R.: On the relationship between subtropical clouds and meteorology in observations and CMIP3 and CMIP5 models, J. Climate, 28, 2945–2967, 2015.

Nam, C., Bony, S., Dufresne, J.-L., and Chepfer, H.: The 'too few, too bright' tropical low-cloud problem in CMIP5 models, Geophys. Res. Lett., 39, L21801, 2012, doi:10.1029/2012GL053421.

Nuijens, L., B. Stevens, and A. P. Siebesma: The environment of precipitating shallow cumulus convection, J. Atmos. Sci.,
10   66, 1962–1979, 2009.

Nuijens, L., and Stevens, B.: The influence of wind speed on shallow marine cumulus convection, J. Atmos. Sci., 69, 168–184, 2012.

Oreopoulos, L., and Cahalan, R. F.: Cloud inhomogeneity from MODIS, J. Climate, 18, 5110–5124, 2005.

Platnick, S., Meyer, K. G., King, M. D., and Coauthors: The MODIS cloud optical and microphysical products: Collection 6
15   updates and examples from Terra and Aqua, IEEE Trans. Geosci. Remote Sens., 55, 502–525, 2017.

Rapp, A. D., Lebsock, M., and T. L'Ecuyer, T.: Low cloud precipitation climatology in the southeastern Pacific marine stratocumulus region using CloudSat, Environ. Res. Lett., 8, 2013, doi:10.1088/1748-9326/8/1/014027.

Richter, I., and Xie, S.-P.: Muted precipitation increase in global warming simulations: A surface evaporation perspective, J. Geophys. Res., 113, D24118, doi:10.1029/2008JD010561, 2008.

20   Rieck, M., Nuijens, L., and Stevens, B.: Marine boundary layer cloud feedbacks in a constant relative humidity atmosphere, J. Atmos. Sci., 69, 2538–2550, 2012.

Rienecker, M. M., Suarez, M. J., Gelaro, R., and Coauthors: MERRA: NASA's Modern-Era Retrospective Analysis for Research and Applications. J. Climate, 24, 3624-3648, doi:10.1175/JCLI-D-11-00015.1, 2011.

Rossow, W. B. and Schiffer, R. A.: Advances in Understanding Clouds from ISCCP, B. Am. Meteorol. Soc., 72, 2–20, 1999.

25   Schreier, M. M., Kahn, B. H., Eldering, A., Elliott, D. A., Fishbein, E., Irion, F. W., and Pagano, T. S.: Radiance comparisons of MODIS and AIRS using spatial response information, J. Atmos. Oceanic Technol., 27, 1331–1342, doi:10.1175/2010JTECHA1424.1, 2010.

Sherwood, S. C., Ingram, W., Tsushima, Y., Satoh, M., Roberts, M., Vidale, P. L., and O'Gorman, P. A.: Relative humidity changes in a warmer climate, J. Geophys. Res., 115, D09104, doi:10.1029/2009JD012585, 2010.

30   Stephens, G. L., Vane, D. G., Boain, R. J., and Coauthors: The CloudSat mission and the A-train, Bull. Amer. Meteor. Soc., 83, 1771–1790, 2002.

Stephens, G. L.: Cloud feedbacks in the climate system: A critical review, J. Climate, 18, 237–273, 2005.

Suselj, K., Teixeira, J., and Chung, D.: A unified model for moist convective boundary layers based on a stochastic eddy-diffusivity/mass-flux parameterization, J. Atmos. Sci., 70, 1929–1953, 2013.

Suzuki, K., Nakajima, T., Nakajima, T. Y., and Khain, A. P.: A study of microphysical mechanisms for correlation patterns between droplet radius and optical thickness of warm clouds with a spectral bin microphysics cloud model, J. Atmos. Sci., 67, 1126–1141, 2010a.

Suzuki, K., Nakajima, T., Nakajima, T. Y., and Stephens, G. L.: Effect of the droplet activation process on microphysical

5   properties of warm clouds, Environ. Res. Lett., 5, 1–6, 2010b, doi:10.1088/1748-9326/5/2/024012.

Teixeira, J., Cardoso, S., Bonazzola, M., and Coauthors: Tropical and subtropical cloud transitions in weather and climate prediction models: The GCSS/WGNE Pacific cross-section intercomparison (GPCI), J. Climate, 24, 5223–5256, 2011.

von Engeln, A., Teixeira, J., and Beyerle, G.: Impact of thin water vapor layers on CHAMP radio occultation measurements, Radio Sci., 42, RS2010, doi:10.1029/2005RS003379, 2007.

10   Weber, T., Quaas, J., and Räisänen, P.: Evaluation of the statistical cloud scheme in the ECHAM5 model using satellite data. Q.J.R. Meteorol. Soc., 137, 2079–2091. doi: 10.1002/qj.887, 2011.

Wood, R., and Bretherton, C. S.: Boundary layer depth, entrainment and decoupling in the cloud-capped subtropical and tropical marine boundary layer, J. Clim., 17, 3576–3588, 2004.

Wood, R., and Hartmann, D. L.: Spatial variability of liquid water path in marine boundary layer clouds: The importance of

15   mesoscale cellular convection. J. Climate, 19, 1748–1764, 2006.

Wood, R., and Field, P. R.: The Distribution of Cloud Horizontal Sizes. J. Climate, 24, 4800–4816. doi: http://dx.doi.org/10.1175/2011JCLI4056.1, 2011.

Wood, R.: Stratocumulus Clouds. Mon. Wea. Rev., 140, 2373–2423. doi: http://dx.doi.org/10.1175/MWR-D-11-00121.1, 2012.

20   Yue, Q., Kahn, B. H., Fetzer, E. J., and Teixeira, J.: Relationship between oceanic boundary layer clouds and lower tropospheric stability observed by AIRS, CloudSat, and CALIOP, J. Geophys. Res., 116, D18212, doi:10.1029/2011JD016136, 2011.

Yue, Q., Kahn, B. H., Xiao, H., Schreier, M. M., Fetzer, E. J., Teixeira, J., and Suselj, K.: Transitions of cloud-topped marine boundary layers characterized by AIRS, MODIS, and a large eddy simulation model, J. Geophys. Res. Atmos., 118,

25   8598–8611, doi:10.1002/jgrd.50676, 2013.

Yue, Q., Kahn, B. H., Fetzer, E. J., Wong, S., Frey, R., and Meyer, K. G.: On the response of MODIS cloud coverage to global mean surface air temperature, J. Geophys. Res. Atmos., 122, 966–979, doi:10.1002/2016JD025174, 2017.

Zelinka, M. D., Klein, S. A., and Hartmann, D. L.: Computing and partitioning cloud feedbacks using cloud property histograms. Part II: Attribution to changes in cloud amount, altitude, and optical depth, J. Climate, 25, 3736–3754, 2012.

30   Zhang, Z., Ackerman, A. S., Feingold, G., Platnick, S., Pincus, R., and Xue, H.: Effects of cloud horizontal inhomogeneity and drizzle on remote sensing of cloud droplet effective radius: Case studies based on large-eddy simulations, J. Geophys. Res., 117, D19208, doi:10.1029/2012JD017655, 2012.

Zhang, Z., Werner, F., Cho, H.-M., Wind, G., Platnick, S., Ackerman, A. S., Di Girolamo, L., Marshak, A., and Meyer, K.: A framework based on 2-D Taylor expansion for quantifying the impacts of subpixel reflectance variance and covariance on

cloud optical thickness and effective radius retrievals based on the bispectral method, J. Geophys. Res. Atmos., 121, 7007–7025, 2016, doi:10.1002/2016JD024837.

Zhao, G., Di Girolamo, L., Diner, D. J., Bruegge, C., J., Mueller, K. J., and Wu, D. L.: Regional changes in Earth's color and texture as observed from space over a 15-year period, IEEE Trans. Geosci. Remote Sens., 54, 4240–4249, 2016.

5   Zhu, P., and Zuidema, P.: On the use of PDF schemes to parameterize sub-grid clouds, Geophys. Res. Lett., 36, L05807, doi:10.1029/2008GL036817, 2009.

Region	Abbrev	Season	Location	% Sc	% Cu	% Other	% Clr	Counts
Northeast Pacific Ocean	NEP	JJA	15°N–35°N 110°W–150°W	23.3	64.8	10.7	1.3	186133
Northeast Atlantic Ocean	NEA	JJA	15°N–35°N 10°W–50°W	8.1	72.0	18.0	1.9	183798
Southeast Pacific Ocean	SEP	SON	5°S–25°S 70°W–110°W	25.5	69.6	3.9	1.0	184208
Southeast Atlantic Ocean	SEA	SON	5°S–25°S 25°W–15°E	31.8	62.1	4.4	1.7	180668

Table 1: The four regions investigated in this study are greatly expanded in area from Klein and Hartmann (1993). The four columns with percentages and total counts are defined at the AIRS/AMSU field of regard (FOR) spatial scale. The three cloudy categories indicate whether clouds of that type occur with any frequency within the AIRS/AMSU FOR. Clear is defined over the entire AIRS/AMSU FOR and are therefore very infrequent.

5
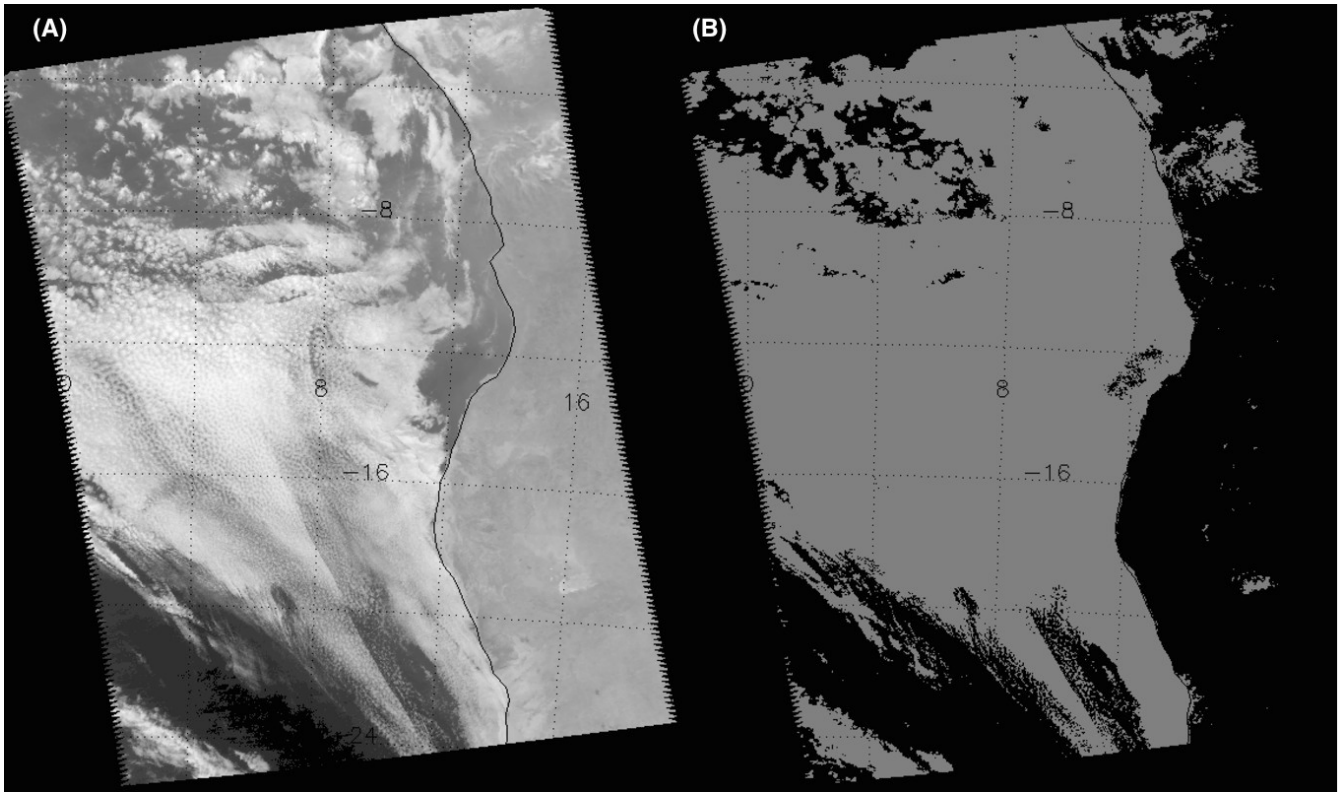
Figure 1. AIRS version 5 visible channel 4 radiance (0.49–0.94 μm) at a nadir spatial resolution of 2.28 km (left), and AIRS cloud mask (binary clear and cloudy) determined from visible channel thresholds (right). See *Gautier et al.* [2003] for more details.

5

21
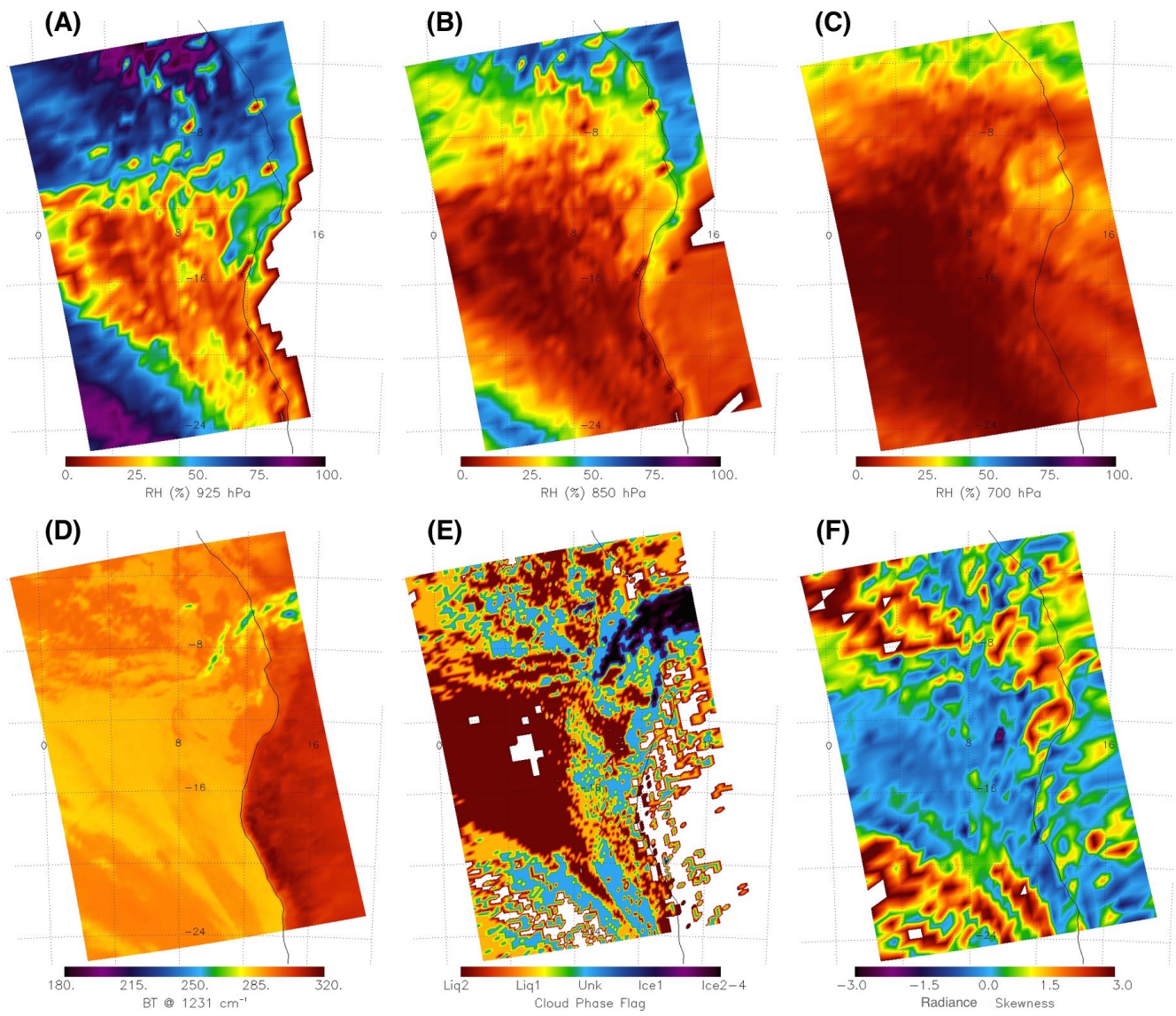
Figure 2. AIRS (a) RH$_{925}$ (%), (b) RH$_{850}$ (%), (c) RH$_{700}$ (%), (d) 1231 cm^{-1} T$_b$ (K), (e) cloud thermodynamic phase, and (f) radiance skewness from visible channel 4. The granule is identical to the one shown in Fig. 1.

5
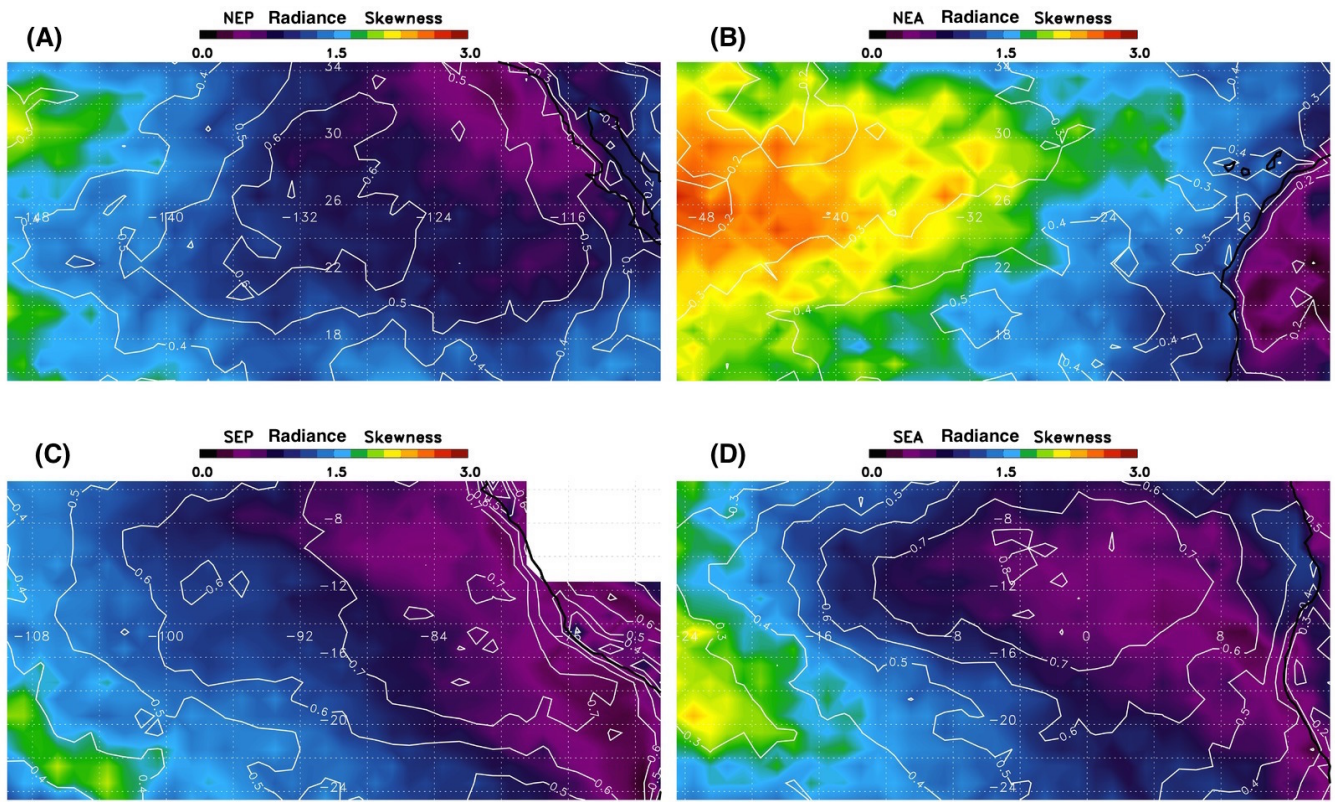
Figure 3. Radiance skewness for regions listed in Table 1: (a) NEP, (b) NEA, (c), SEP, and (d) SEA. The AIRS ECF is overlaid as white contours.

Figure 4. MBL depth (hPa) for regions listed in Table 1: (a) NEP, (b) NEA, (c), SEP, and (d) SEA. The AIRS 1000-700 hPa dMSE is overlaid in white contors (solid are for positive and dashed for negative).
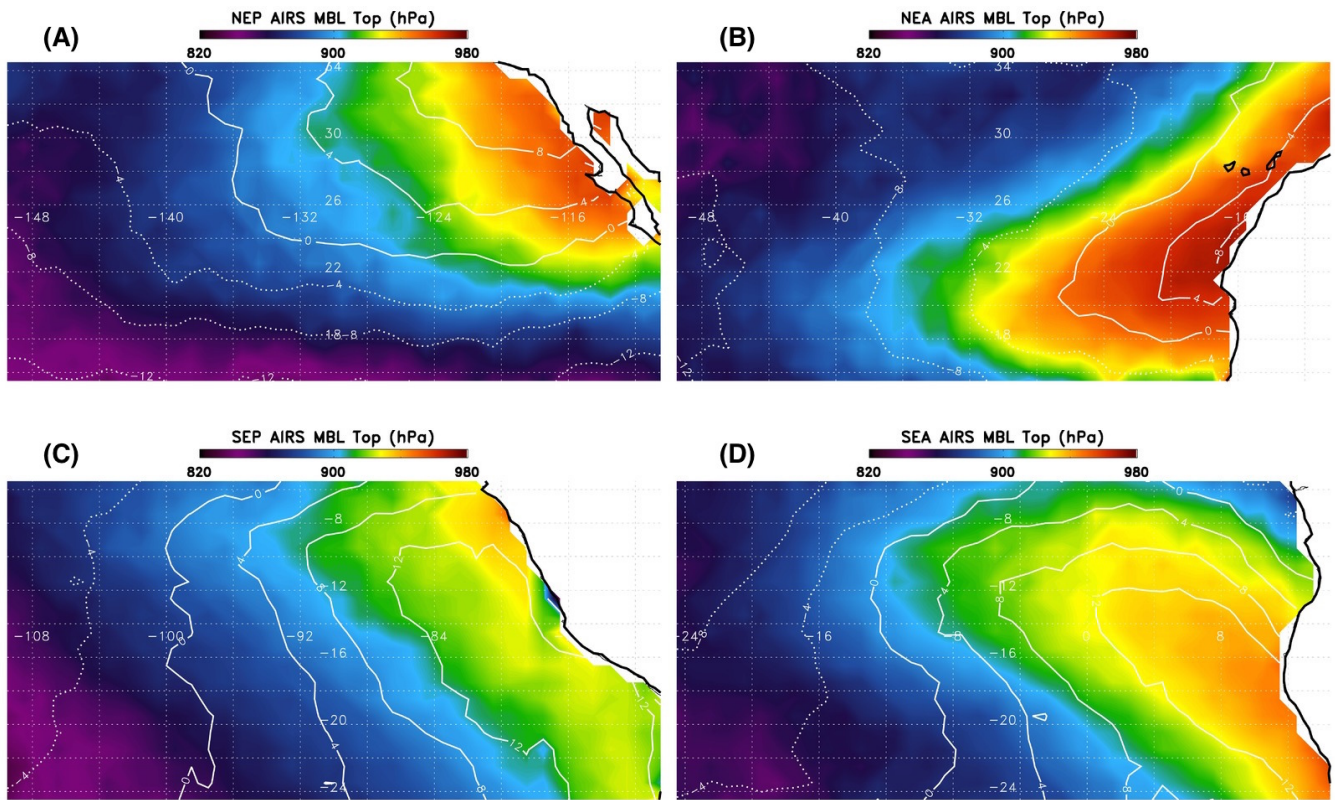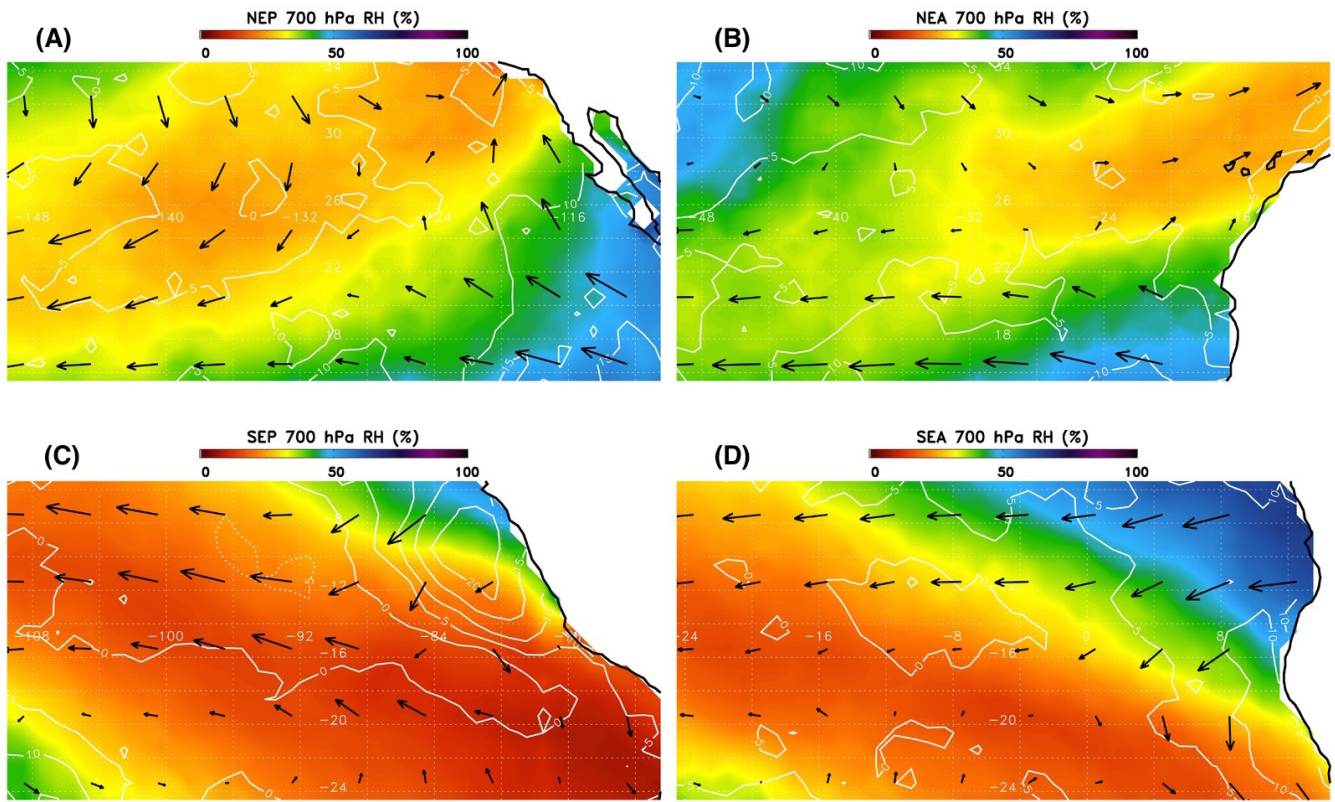
Figure 5. AIRS RH$_{700}$ (%) for regions listed in Table 1: (a) NEP, (b) NEA, (c), SEP, and (d) SEA. The MERRA-AIRS RH$_{700}$ difference is shown as white contours (solid implies MERRA is moister, and dashed implies AIRS is moister). The length and direction of the arrows depict the 700 hPa wind vectors from MERRA.

25
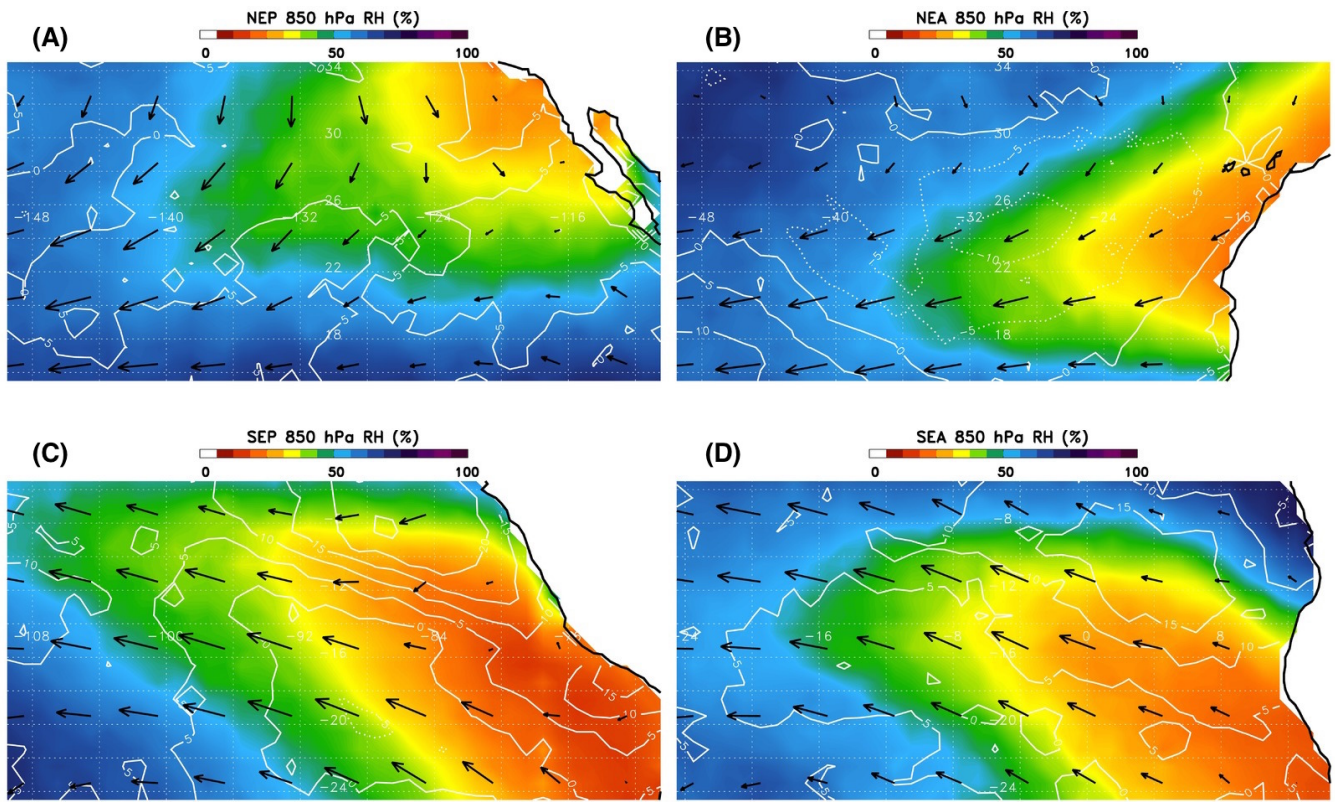
Figure 6. AIRS RH$_{850}$ (%) for regions listed in Table 1: (a) NEP, (b) NEA, (c), SEP, and (d) SEA. The MERRA-AIRS RH$_{850}$ difference is shown as white contours (solid implies MERRA is moister, and dashed implies AIRS is moister). The length and direction of the arrows depict the 850 hPa wind vectors from MERRA.

26

Figure 7. Shown are joint pdfs for six different combinations of variables that are described in Section 4.2: (a) radiance versus AIRS ECF, (b) radiance versus MODIS CF, (c) MODIS τ versus AIRS ECF, (d) MODIS τ versus MODIS CF, (e) radiance versus MODIS τ, and (f) MODIS CF versus AIRS ECF. The grey scale is the natural log of total counts per bin. All values in the pdfs shown are for the cumulus regime. The color contours depict the MBL depth (hPa).

Figure 8. Joint pdfs of visible radiance versus ECF for the four spatial regions listed in Table 1. The SEP in Fig.7 is repeated here for clarity.

5
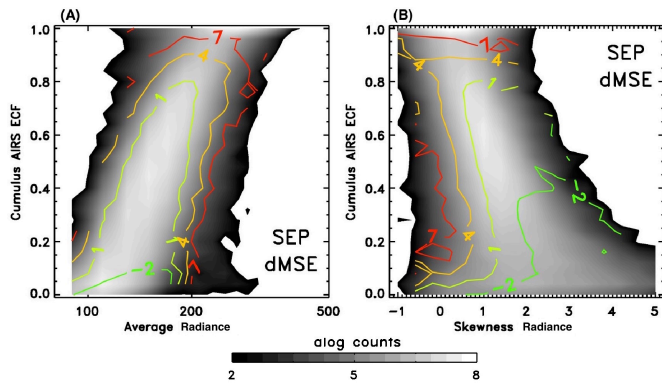
Figure 9. Joint pdfs of visible radiance average (left) and skewness (right) versus ECF for the SEP with dMSE depth as the overlay field. Other regions are very similar and are not shown for reasons of brevity.
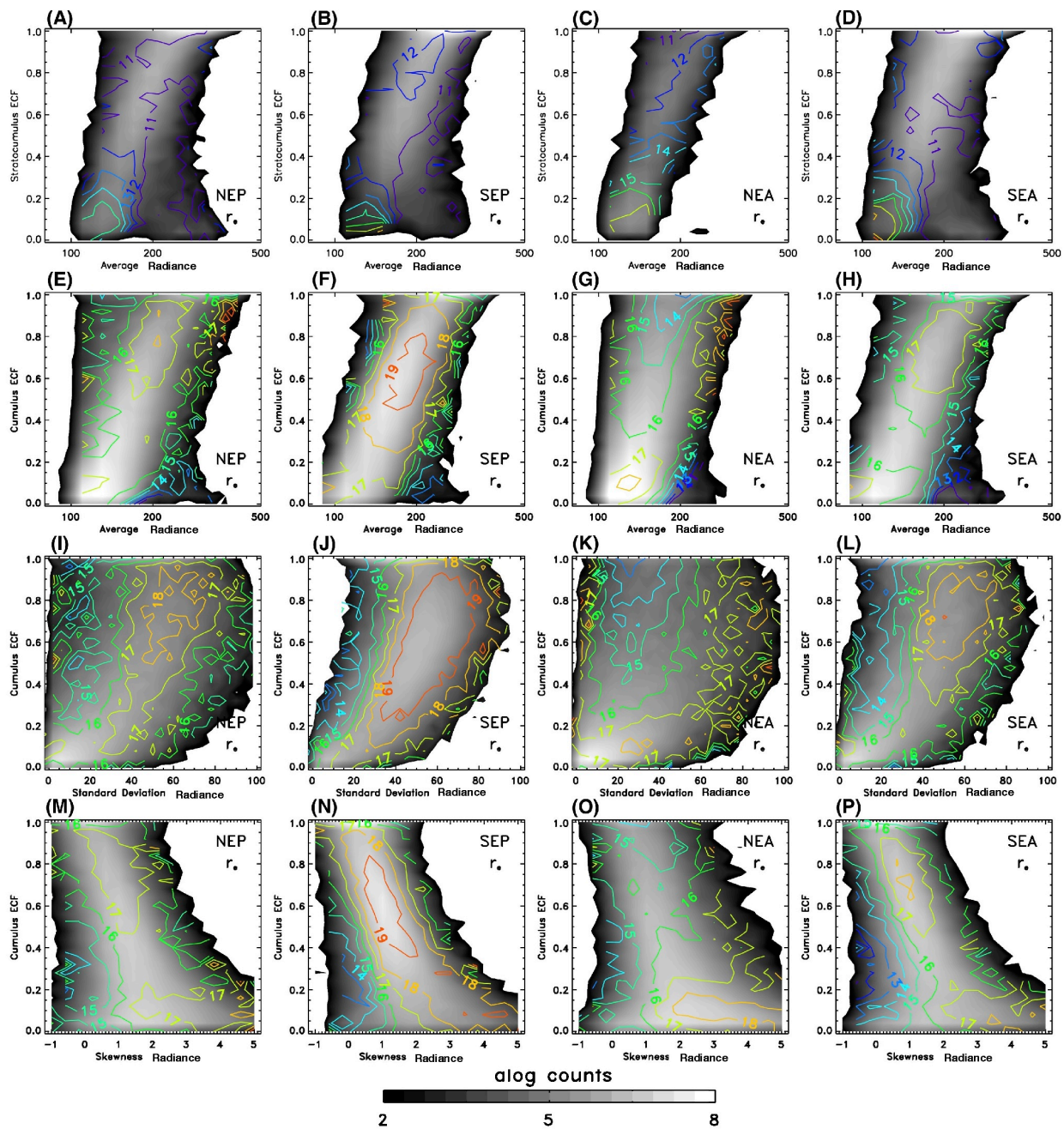
Figure 10. Joint pdfs of visible radiance skewness versus ECF for the four regions listed in Table 1, and the overlay field is r_e.
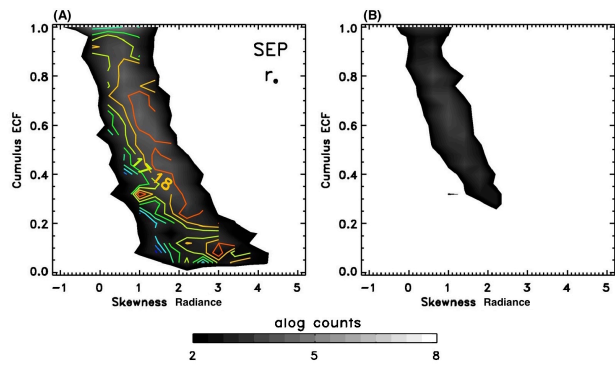
Figure 11. (a) Same as Fig. 10n except sampling restricted to AMSU FORs that contain the CloudSat ground track. (b) Samples of the data in (a) that contain detected precipitation according to CloudSat.

31
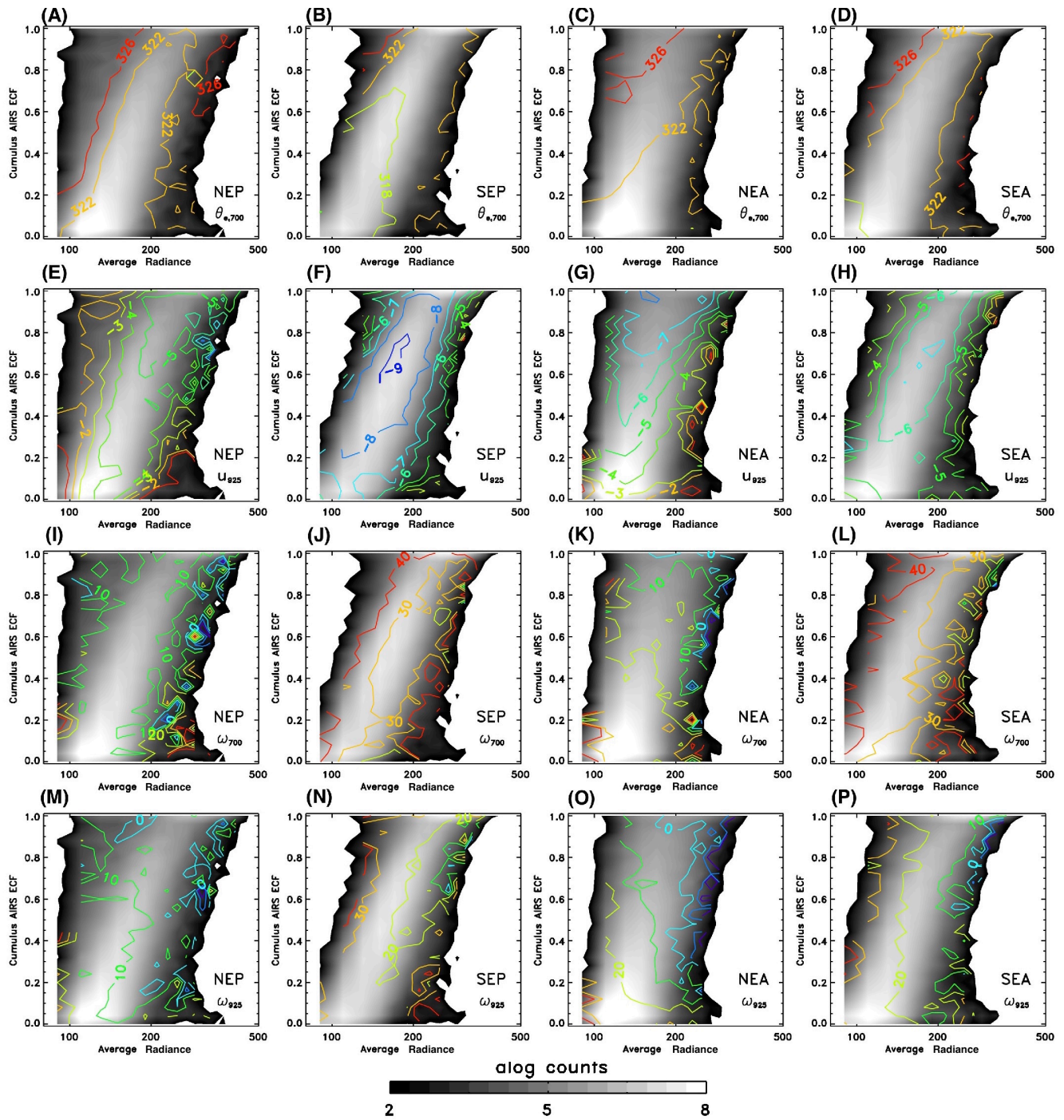
Figure 12. Joint pdfs of 700 hPa θ_e, u_{925}, ω_{700}, and ω_{925} for the four regions listed in Table 1.